A&A, 715, A150 (2026)
https://doi.org/10.1051/0004-6361/202660524
© The Authors 2026

Astronomy & Astrophysics

The oldest low-α thin disc stars

Riano E. Giribaldi[1,⋆], Laura Magrini[1], Marco Palla[1], and Carlos Viscasillas Vázquez[1,2]

[1] INAF – Osservatorio Astrofisico di Arcetri, Largo E. Fermi 5, 50125 Firenze, Italy
[2] Institute of Theoretical Physics and Astronomy, Faculty of Physics, Vilnius University, Sauletekio av. 3, 10257 Vilnius, Lithuania

Received 21 April 2026 / Accepted 12 September 2026

ABSTRACT

The formation pathway of the α-poor Milky Way (MW) thin disc remains under debate. The latest observational data indicates the presence of comparable numbers of old stars in both the low- and high-α disc components, suggesting either coeval or overlapping formation epochs. Using GALAH DR4, we provide evidence that α-poor stars have coexisted with α-rich stars since ∼12.5 Gyr ago. Stellar ages of 0.5 Gyr precision were re-derived for nearly 30 000 subgiant stars using accurate effective temperatures ($T_{\rm eff}$) from the infrared flux method (IRFM) together with distances based on Gaia parallaxes. About 22% of the sample constitutes a population peaking at 9.2 Gyr, with evidence for an extended old-age tail reaching 12.5 Gyr. Among stars older than 10 and 11 Gyr, between 20 and 30% have relative low [α/Fe] and solar-like metallicities ($-0.5 \leq$ [Fe/H] $\leq +0.5$ dex). These stars exhibit kinematics consistent with those of near solar-age α-poor stars in the thin disc. These stars can be evolved Sun-like stars, i.e. old solar analogues, whose $T_{\rm eff}$ and gravity modified with time. Comparison with a well-tested Galactic disc chemical evolution model supports the presence of a significant fraction of old, α-poor disc stars, confirming the plausibility of our selection criteria. We provide a catalogue with the selected sample to facilitate spectroscopic follow-ups at high resolution.

Key words. stars: abundances – stars: fundamental parameters – Galaxy: disk – Galaxy: evolution – Galaxy: general – Galaxy: kinematics and dynamics

1. Introduction

Evidence for the existence of galaxies with solar or near-solar metallicities within the first ∼2.5 Gyr of cosmic history has steadily accumulated over the last two decades (e.g. Maiolino et al. 2008; Savaglio et al. 2012; Sommariva et al. 2012; Scholte et al. 2025; Faisst et al. 2026). These observations imply that efficient chemical enrichment can occur on relatively short timescales, leading to chemically mature stellar populations at epochs traditionally associated with predominantly metal-poor environments. If similar enrichment processes occurred in the MW, they raise fundamental questions about how rapidly the chemical conditions required to produce solar-metallicity stars can be established, and hence how early environments favourable to the formation of terrestrial planets may have emerged (see, e.g. Spitoni et al. 2025).

Evidence of the existence of old metal-rich stars in the MW was scarce in the past, as relatively few near-solar metallicity stars older than ∼10 Gyr were known prior to the *Gaia* era. Before *Gaia*, only a few hundred main-sequence turnoff (MSTO) and subgiant branch (SGB) stars with sufficiently precise distances and spectroscopic measurements enabling reliable age determinations were available (e.g. Nordström et al. 2004; Haywood et al. 2013; Mitschang et al. 2014; Bensby et al. 2014. These samples have been extensively used to construct and refine theoretical models of the MW's disc structure, in particular the formation of the thin and thick discs. The thin disc is characterised by relatively low [α/Fe] abundances (hereafter α-poor; typically defined averaging [Mg/Fe], [Si/Fe], [Ca/Fe], and [Ti/Fe]). On this basis, several studies have supported a scenario in which a thick α-rich disc is confined to the inner Galaxy, this is, within a Galaxy radius ($R_{\rm Gal}$) approximately lower than 9 kpc. In that region, the gas is progressively diluted by the accretion of more metal-poor material from the outer disc, leading to the formation of a distinct thin disc, characterised by a different chemical composition and spatial distribution (e.g. Hayden et al. 2015; Snaith et al. 2015; Haywood et al. 2018, 2019; Katz et al. 2021).

Today, *Gaia* and large photometric and spectroscopic surveys are providing a whole set of information required to disentangle the origin of the Galactic stellar populations. The stellar ages of hundreds of thousands of MSTO and SGB stars were estimated providing a chronological timeline of the assembling history of the Galaxy (e.g. Sharma et al. 2018; Xiang & Rix 2022; Ciucă et al. 2021, 2024; Gent et al. 2024; Nepal et al. 2024; Gallart et al. 2024). Indeed, MSTO and SGB stars are particularly valuable because their widely separated isochrones allow stellar ages to be determined with the highest precision. In particular, Beraldo e Silva et al. (2021); Nepal et al. (2024) and Borbolato et al. (2025) showed that the thin disc might host a significant number of stars older than ∼10 Gyr, including a few ones with solar metallicity. However, owing to their faintness, these stars have not yet been subject to detailed spectroscopic analyses capable of probing the nucleosynthetic processes at the onset of thin-disc formation.

The uniqueness of the Sun and its planetary system relative to the broader diversity of stellar systems remains an open question, although the rapidly growing census of exoplanets is increasingly placing the Solar System in a Galactic context (e.g. Adibekyan 2019; Tsantaki et al. 2026). Therefore, it is crucial to establish since when Sun-like stars started to form because it constrains the emergence of solar-metallicity conditions in the MW, and thus constrains timescales for the appearance of Earth-like planets. In the search for stars that may resemble a newborn Sun at the earliest epochs of the Galactic thin disc, we selected a

⋆ Corresponding author: riano.escategiribaldi@inaf.it

Open Access article, published by EDP Sciences, under the terms of the Creative Commons Attribution License (https://creativecommons.org/licenses/by/4.0), which permits unrestricted use, distribution, and reproduction in any medium, provided the original work is properly cited.
This article is published in open access under the Subscribe to Open model. Subscribe to A&A to support open access publication.

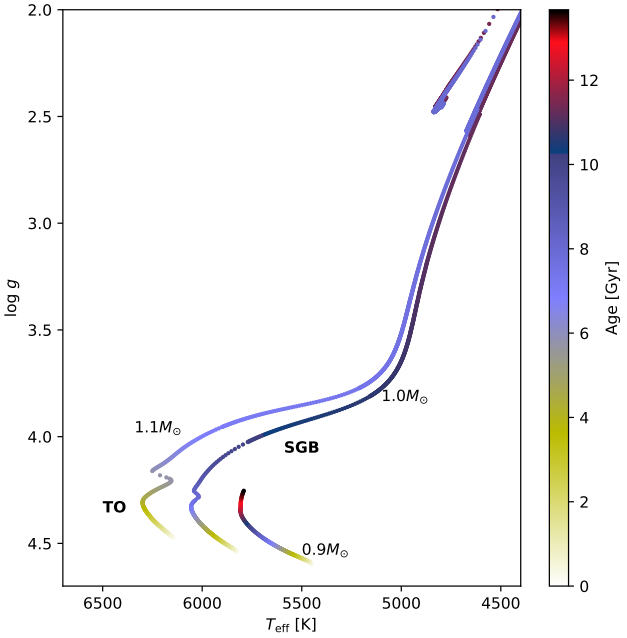

Fig. 1. Evolutionary paths of Sun-like stars. BASTI evolutionary tracks (Hidalgo et al. 2018) of [Fe/H] = −0.08 dex and [α/Fe] = 0 dex, for stars with 0.9 $M_\odot$, 1 $M_\odot$, and 1.1 $M_\odot$ are shown. Age was truncated up to the age of the universe 13.7 Gyr (Planck Collaboration VI 2020).

sample of very old subgiant stars, for which age determinations are among the most precise currently achievable, with kinematics consistent with thin-disc membership and metallicities close to the solar value. These objects constitute candidate old solar analogues. Namely, whereas solar analogues simply refer to stars with atmospheric parameters similar to those of the Sun (e.g. Hardorp 1978; Cayrel de Strobel 1996; Porto de Mello et al. 2014), we call old solar analogues those stars older than ∼10 Gyr that shared approximately the same parameters with the Sun at their zero-age main-sequence stage. Their existence would indicate that stars with solar-like properties were already present during the earliest phases of thin-disc formation, as suggested by recent evidence for ancient solar-metallicity thin-disc populations (e.g. Nepal et al. 2024; Borbolato et al. 2025). Such stars have evolved only slightly from their zero-age position in the Kiel diagram. For example, a solar-mass star (1 $M_\odot$) leaves the main sequence and reaches the subgiant branch after about 10 Gyr, as Fig. 1 shows (see, also, Bressan et al. 2012), while largely preserving its initial photospheric chemical composition. Consequently, selecting stars at the SGB region shown in Fig. 1 provides a sample of stars with initial masses of approximately 0.9–1.0 $M_\odot$, for which precise ages can be inferred from their well-separated isochrones.

In this work, we present a selection of α-poor stars older than 10 Gyr from the GALactic Archaeology with Hermes Data Release 4 (GALAH DR4) survey (Buder et al. 2025), chosen as candidates for detailed chemical characterization. Our selection combines chemical and dynamical criteria. Surface gravities ($\log g$) and ages were re-derived for SGB stars using validated effective temperatures ($T_{\rm eff}$) and precise distances based on *Gaia* parallaxes. Our method, which is dependent on stellar evolutionary models, was validated using the old globular cluster NGC 6352 with moderate metallicity [Fe/H] = −0.55 (Feltzing et al. 2009), ensuring that no bias affects the inferred ages of field stars.

This paper is structured as follows. Section 2 presents our data selection using GALAH catalogues. It involves our own age estimates, the method for which is described in detail. A validation of the method with the old stellar cluster NGC 6352, with stars of similar parameters to those searched in this investigation, is presented in the Appendix. Section 3 shows the characterisation of the selected old stars, where the separation of thin- and thick-disc disc stars is observed by means of chemical and orbital criteria. Section 4 shows a comparison between observational data and predictions of chemical evolution models. Finally, Section 5 presents our conclusions.

2. Data sample

2.1. Initial selection of thin disc stars

The primary goal of this work is to identify the old population of the Galactic thin disc and to derive stellar ages with the highest precision achievable through isochrone fitting, which is maximised for MSTO and SGB stars. The initial sample is based on the GALAH DR3 catalogue (Buder et al. 2021), with subsequent improvements from GALAH DR4 (Buder et al. 2025), which builds on Gaia DR3 (Gaia Collaboration 2018) and incorporates an improved treatment of source cross-matching and binary systems. As a consequence, a number of stars classified as non-single in Gaia DR3 were removed in GALAH DR4.

GALAH DR3 includes the largest subset of stars with $T_{\rm eff}$ derived via the infrared flux method (IRFM, Blackwell et al. 1979, 1980) implemented for Gaia and 2MASS photometry (Casagrande et al. 2021), the accuracy of which is based on the validations of Casagrande et al. (2006) and Casagrande et al. (2010). Owing to its robust zero-point calibration and its near model-independence, IRFM $T_{\rm eff}$ estimates together with those from interferometric angular diameters[1] (e.g. Bazot et al. 2011; Karovicova et al. 2020) and eclipsing binaries (e.g. Miller et al. 2020; Maxted et al. 2022) constitute primary calibration standards (e.g. Heiter et al. 2015; Zwintz et al. 2026), as $T_{\rm eff}$ strongly influences all other stellar parameters.

Since our stellar classification is critically dependent on the accuracy of the age estimates and thus on $T_{\rm eff}$, we adopted the IRFM temperatures from GALAH DR3 for the GALAH DR4 sample throughout the subsequent analysis. This combination of DR3 temperatures with DR4 abundances is justified by the good compatibility between the $T_{\rm eff}$ scales of the two catalogue releases. The DR4 temperatures are calibrated against the *Gaia* Benchmark Stars (Heiter et al. 2015), whose temperature scale is consistent with the IRFM scale (Giribaldi et al. 2021, 2023). Thus, combining the DR3 IRFM $T_{\rm eff}$ scale with the DR4 chemical abundances should not introduce a significant systematic inconsistency. At the same time, DR4 provides more precise elemental abundances than DR3, owing to the greater number of spectral lines used in their determination. Therefore, we adopted the DR3 IRFM temperatures together with the DR4 abundances throughout our analysis, thereby retaining the well-established IRFM $T_{\rm eff}$ scale while taking advantage of the improved precision of the DR4 chemical abundances. Appendix A shows the compatibility of the $T_{\rm eff}$ and $\log g$ scales related to the ages in this work with those of GALAH DR4.

We further restricted the sample to disc kinematics by selecting stars located in the prograde region of the Lindblad diagram (orbital energy versus angular momentum L_Z), following the

[1] Many of them compiled in the *Gaia* Benchmark Stars sample (Heiter et al. 2015; Soubiran et al. 2024).

global separation illustrated in Fig. 4 of Giribaldi & Smiljanic (2023). We then imposed quality cuts on atmospheric parameters and parallaxes, requiring `flag_fe_h = 0`, `flag_alpha_fe = 0`, and `flag_sp = 0`, and selecting stars with $\varpi \geq 0.7$ mas and $\varpi/\sigma(\varpi) > 5$ to ensure the determination of reliable distances. To focus on MSTO and SBG stars, we further applied $T_{\rm eff} < 6750$ K to exclude hot young stars, $\log g < 4.4$ dex to maintain the regime where our isochrone-based gravity estimates remain reliable, and $-1.5 <$ [Fe/H] $< +0.45$ dex. These criteria result in a sample of 166 441 stars, spanning a wide range of ages and covering the full metallicity distribution of the Galactic thin disc.

2.2. Stellar age determination

We derived stellar ages using the Python code q^2 (Ramírez et al. 2014), which performs a frequentist inference framework (as implemented in Ramírez et al. 2013) based on the input quantities $T_{\rm eff}$, [Fe/H], extinction-corrected V band magnitude (V_0), and parallax ϖ, along with their respective uncertainties. The code inverts the parallax to compute distances and derive absolute magnitudes (M_V), which provide a good approximation for nearby stars. For $\varpi \lesssim 1.3$ mas, this approximation may introduce small biases; therefore, we instead adopt the geometric distances from Bailer-Jones et al. (2021), which include corrections for the *Gaia* parallax zero-point offset (Lindegren et al. 2021).

The code employs Yale–Yonsei isochrones (Kim et al. 2002; Yi et al. 2003) of solar-scaled composition, sampled in metallicity with 0.02 dex spacing. To account for α-enhancement effects, we follow the approach of Spina et al. (2018), which maps [α/Fe] to an effective metallicity using the prescription of Salaris et al. (1993):

$$[\mathrm{M/H}] = [\mathrm{Fe/H}] + \log(0.638 \times 10^{[\alpha/\mathrm{Fe}]} + 0.362) \quad (1)$$

where the average of [Mg/Fe], [Si/Fe], [Ca/Fe], and [Ti/Fe] is adopted as [α/Fe]. As shown by Spina et al. (2018); Xiang & Rix (2022) and Viscasillas Vázquez et al. (2026), this correction avoids systematic age biases of 1–2 Gyr that mainly affect stars older than ∼8 Gyr. We also apply a zero-point correction of +0.04 dex (i.e. an offset of −0.04 dex is assumed) in [M/H] to account for the effects of atomic diffusion at solar parameters (Meléndez et al. 2012; Dotter et al. 2017), which allows recovery of the solar age of 4.6 Gyr (Connelly et al. 2008; Amelin et al. 2010) inferred from fundamental parameter constraints.

The method is validated in Appendix B with the old globular cluster NGC 6352, while its sources of uncertainty and potential biases are examined in Appendix C. The method returns posterior probability distributions for $\log g$, age, mass, luminosity, and radius. Our analysis indicates that the age uncertainties are dominated by the combined effects of $T_{\rm eff}$ and M_V uncertainties, with the latter incorporating contributions from the photometric magnitude, reddening, and parallax uncertainties. The age precision improves significantly for SGB stars compared to TO stars, as the sensitivity of the derived age to deviations in $T_{\rm eff}$ from its true value becomes negligible at this evolutionary stage. A detailed analysis of these effects is presented in Appendix C.

Uncertainties in IRFM $T_{\rm eff}$ are assumed to be 70 K, obtained by combining in quadrature the intrinsic scatter and zero-point uncertainty of the colour–$T_{\rm eff}$ calibrations (60 K and 20 K, respectively; Casagrande et al. 2021). Parallax uncertainty is adopted from the Gaia catalogue, which for our stars is statistically equivalent to to that obtained by propagating the uncertainty in the geometric distance. The uncertainty of V_0 is dominated by two sources that were added in quadrature. These are, the uncertainty of the Gaia–Johnson transformation given in Eq. (D.1) ($\sigma(V_{calib}) = 0.03$ mag) and the uncertainty of extinction correction. For the latter, the uncertainty given by Eq. (D.2) is scaled to the V band using the standard coefficient $R_V = 3.1$. A robust assessment of the reddening uncertainties is essential for evaluating their contribution to the age error budget and identifying potential systematic biases. This analysis is presented in Appendix D, where we find that any systematic effects associated with the adopted reddening, if present, are expected to become significant primarily for stars in regions with $E(B-V) \gtrsim 0.2$. Such effects would concern only a marginal fraction (5–10%) of the stars older than 10, 11, and 12 Gyr, and would bias the inferred ages towards younger or older values if $E(B-V)$ were underestimated or overestimated, respectively.

2.3. Selection of the oldest disc populations

We restricted the sample of 166 441 stars to those with $T_{\rm eff} < 6100$ K. This limit corresponds approximately to the main-sequence turnoff temperature of a 5-Gyr population at solar metallicity and therefore excludes younger, more massive stars. The algorithm for age determination processed data from 91425 stars and converged for 90 099. Of these, 52 815 have internal[2] age uncertainties smaller than 1.5 Gyr; this corresponds to both the 16th and 84th percentiles of their age posterior distributions (σ-like errors henceforth). Figure 2 illustrates the changes in inferred ages induced by typical variations in $T_{\rm eff}$, V_0, [Fe/H], and parallax.

To minimise spurious age overestimates, we applied the prescription established in Appendix C. That is, we first retained stars with $\log g \leq 4.1$ dex (30 972 stars), and subsequently selected only those located within the SGB region of the M_V–$T_{\rm eff}$ diagram. Figure 3 illustrates the latter restriction, where an empirical cut is defined. The colour code clearly exhibits stars older than 10 Gyr on the SGB traced by the isochrones. This cut retained 29 098 stars; we refer to this subset as the characterised sample, which forms the basis of the analysis below. Figure 2 shows that, for these stars, the combined effect of typical uncertainties in the input parameters leads to age uncertainties of ∼0.5 Gyr. Appendix E compares our age estimates with the catalogued ones.

The top panel in Fig. 4 shows the normalised age distribution of the characterised sample, while the bottom panel shows the distribution of the star-by-star σ-like errors. A multi-modal fit reveals a prominent population centred at 9.2 Gyr, whose Gaussian component comprises 22.31% of the sample (6492 stars) and extends to ≈12.5 Gyr at 3σ. Two additional components are identified at younger ages, centred at 6.8 Gyr (Young 1) and 5.1 Gyr (Young 2), typically associated with the thin disc in the literature.

To evaluate the robustness of the oldest tail of the age distribution given the individual age uncertainties, we estimated the expected contribution from stars scattered to older ages. For each star with a measured age below a given threshold (τ_{up}), we used Monte Carlo simulations to sample its age posterior, adopting a Gaussian distribution with an upper uncertainty corresponding to the 84th percentile, and calculated the probability of its age exceeding τ_{up}. Summing these probabilities provides an estimate of the expected number of stars scattered above each threshold.

[2] Uncertainty outcome of the statistical method.

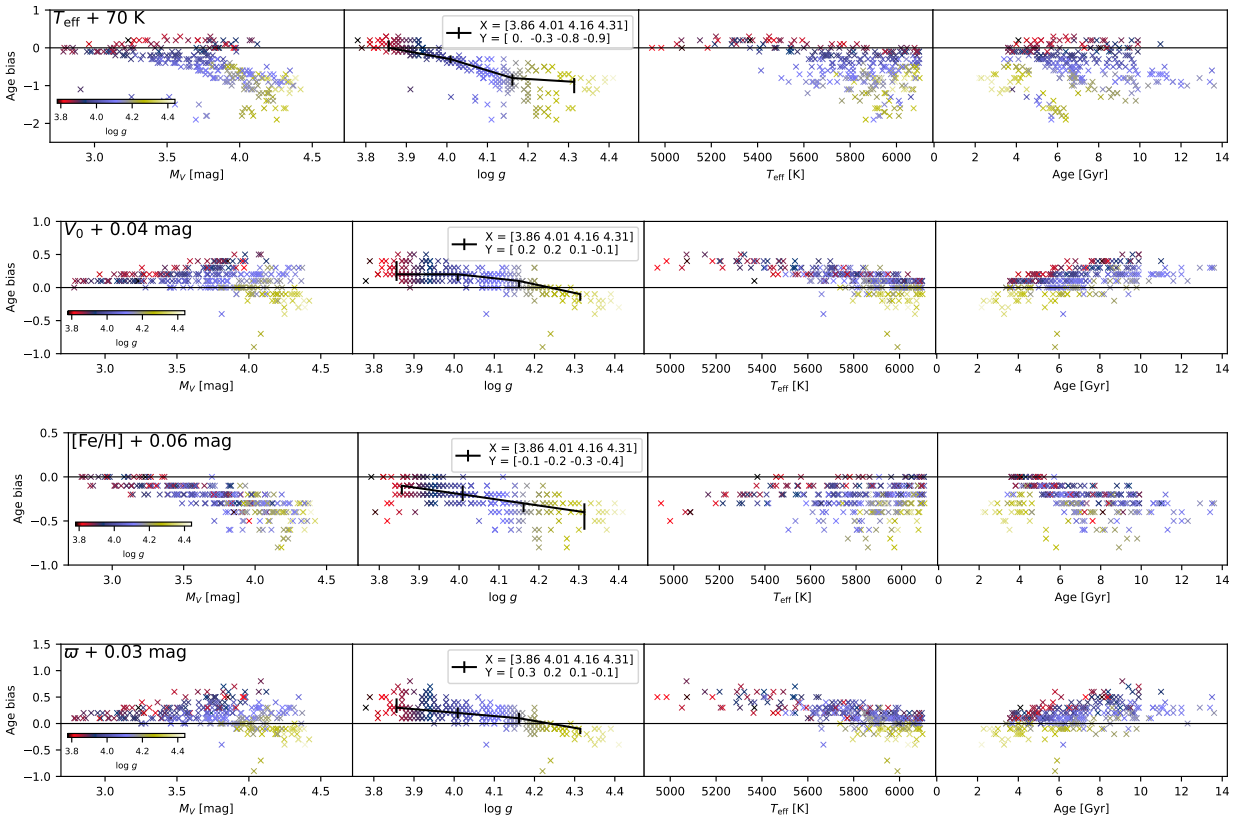

Fig. 2. Correlation between age biases and relevant stellar parameters. From top to bottom, the panels show the response of the age biases to typical variations in $T_{\rm eff}$, V_0, [Fe/H], and parallax, as indicated in the left column. In the panels showing the age bias as a function of log g, the trends are defined by median values computed in equally spaced bins and connected by lines; corresponding quantities are noted in the legends. The sample used corresponds to 300 stars randomly selected from the sample of 52 815 stars, see main text.

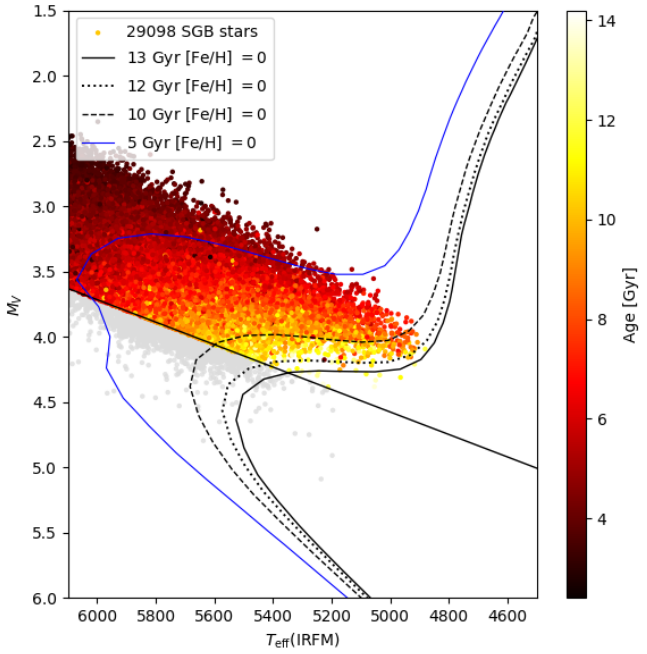

Fig. 3. M_V–$T_{\rm eff}$ diagram of the 35 879 field stars with log $g < 4.1$ dex. The 32 632 stars retained for the age analysis, corresponding to the SGB selection, are colour-coded by age. Stars excluded by the relation $M_V \geq -0.00086\ T_{\rm eff} + 8.876$ (black line) are shown in grey. Yale–Yonsei isochrones with ages and metallicities according to the labels are shown as reference.

Table 1. Expected contribution of age uncertainties to the old-age tail.

τ_{up} (Gyr)	Observed stars	Expected upward-scattered stars	Expected/observed (%)
10.0	1690	496	29
10.5	879	398	45
11.0	452	262	58
11.5	212	163	77
12.0	112	92	82
12.5	68	50	73
13.0	31	32	105

Notes. First column lists the age threshold. Second column displays the number of stars in the characterised sample with ages over the threshold. Third column lists the number of stars scattered over the threshold computed by Monte Carlo simulations. Last column lists percentage of potential age contaminants over the threshold.

Table 1 shows that this contribution becomes increasingly important towards older ages, closely approaching ∼100% for beyond 13 Gyr. The closer the values are to 100%, the better the number of stars above a given τ_{up} is explained by the dispersion due to the age precision. For stars older than 11.5, 12, and 12.5 Gyr, the corresponding ratios are ∼75%. Thus, the expected upwards scattering accounts for most, but not all, of the stars above these age thresholds, with the remaining ∼25% suggesting the presence of a genuine old population. Above 13 Gyr, the expected contribution of 32 stars is consistent with the entire observed sample of 31 stars.

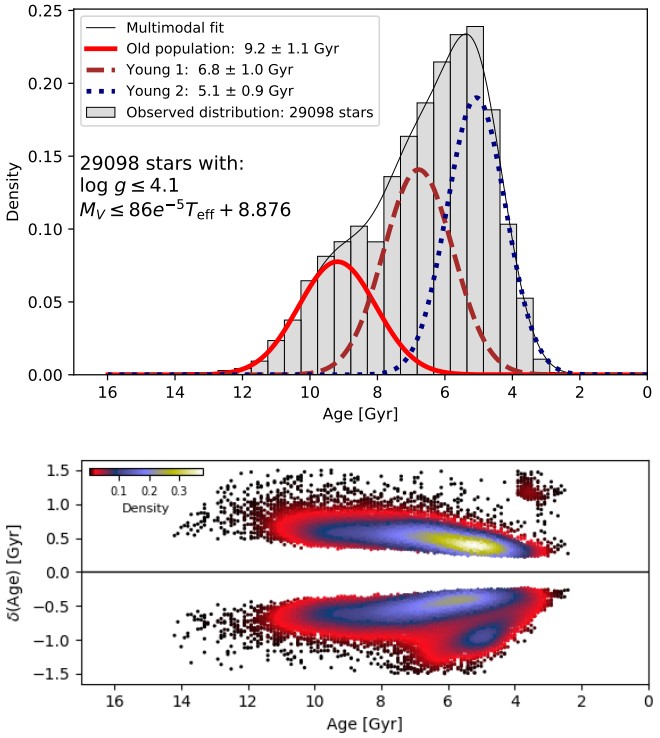

Fig. 4. *Top panel*: age-normalised histogram of the characterised sample. The age axis is segmented into bins of 0.48 Gyr. A multi-modal fit is displayed by the black thin line, the individual distributions of which are represented according to the legends. Each population is labelled by its nickname. Their medians and corresponding σ dispersions are also indicated. *Bottom panel*: σ-like errors of the ages of the stars that compose the histogram on the top panel.

3. Characterisation of the data sample

3.1. Chemical properties

We identified stellar populations belonging to the α-poor and α-rich discs using the most sensitive chemical discriminants, [Mg/Fe] and [Ti/Fe], while we find that other α-elements such as Si and Ca are less effective, as commonly reported in the literature (e.g. Nissen & Schuster 2010; Vincenzo et al. 2021; Buder et al. 2025). Figures 5 and 6 show the oldest stars in the sample in the [Mg/Fe]–[Fe/H] and [Ti/Fe]–[Fe/H] planes, where we grouped them into age intervals. The right-hand panels include thin-disc stars with solar ages (Young 1 population; blue symbols) to highlight their overlap with the old low-α population. The corresponding abundance trends are represented using the 16th, 50th, and 84th percentiles.

The three oldest age intervals show the coexistence of both α-rich ([Mg/Fe] $\gtrsim$ 0.2 dex) and α-poor ([Mg/Fe] $\lesssim$ 0.2 dex) populations with comparable numbers of stars, even at ages exceeding 11 Gyr. The α-poor stars overlap with the sequence of solar-age thin disc stars at solar metallicity regardless of their ages. The presence of such old, chemically thin-disc-like stars is consistent with scenarios in which the thin and thick discs formed contemporaneously during the early evolution of the MW (e.g. Grisoni et al. 2026). Furthermore, the existence of α-poor stars older than 11 Gyr with near-solar metallicities is in line with observations of massive galaxies already reaching near-solar metallicities at redshifts $z \gtrsim 3$ (e.g. Maiolino et al. 2008; Savaglio et al. 2012; Sommariva et al. 2012; Scholte et al. 2025; Faisst et al. 2026).

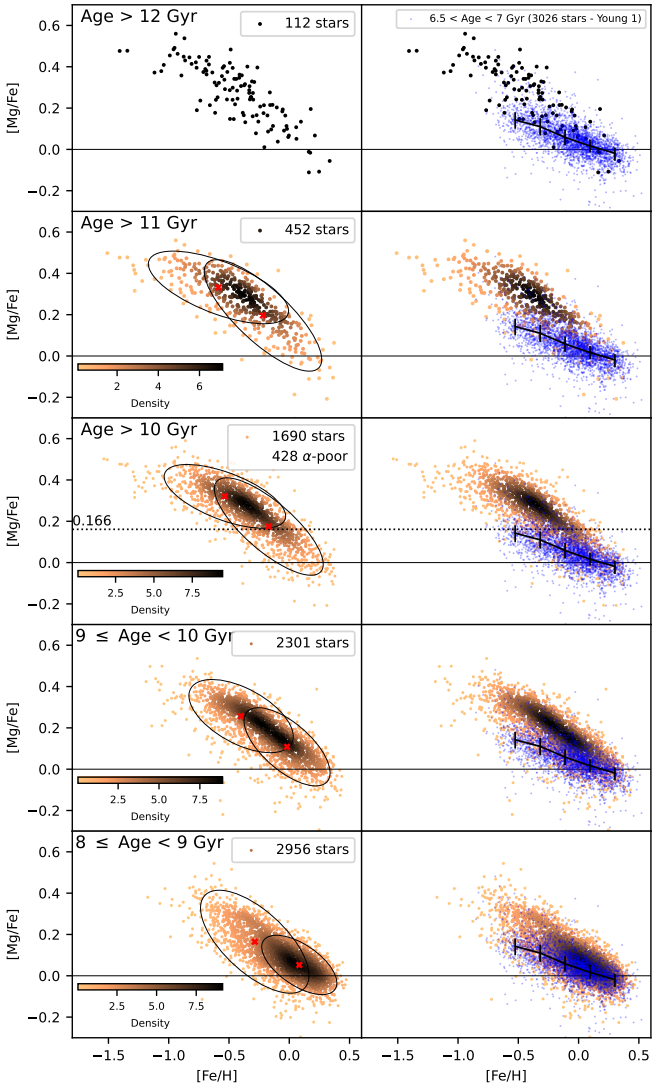

Fig. 5. [Mg/Fe] versus [Fe/H] diagrams. Each row exhibits old stars of three different age ranges, colour-coded according to their probability density scaled in the bars. *Left panels*: ellipses denote the 2σ (~95% probability) contours of the 2D Gaussian-mixture models fitted to the data distributions; red crosses mark their centres. The dotted lines indicate the lower boundaries of the high-α population ellipses. *Right panels*: same distributions as in left panels are shown. Blue dots represent stars of the *Young 1* population (cut of 6.5 ≤ age ≤ 7 Gyr) in Fig. 4. Black lines connect medians of [Mg/Fe] of the blue dots computed in equally separated bins. Vertical bars represent 25 and 75% quartiles around the medians.

To select the stars with the highest probability of being α-poor, we applied Gaussian mixture models (Pedregosa et al. 2011). Figures 5 and 6 show that the abundance distributions of stars older than 10 and 11 Gyr are similar. In both cases, the region most likely associated with α-poor stars lies below the lower boundary of the α-rich component, as defined by the Gaussian ellipses (horizontal dotted lines). These boundaries in both the [Mg/Fe] and [Ti/Fe] planes are nearly consistent and align with the upper envelope of the solar-age thin-disc sequence in blue. We classify as old α-poor (old α-rich) the stars that consistently lie below (above) the dotted boundaries in the third-row panels of Figs. 5 and 6. Of the 1690 stars older than 10 Gyr, 364 are classified as α-poor and 1134 as α-rich, while 192 stars show

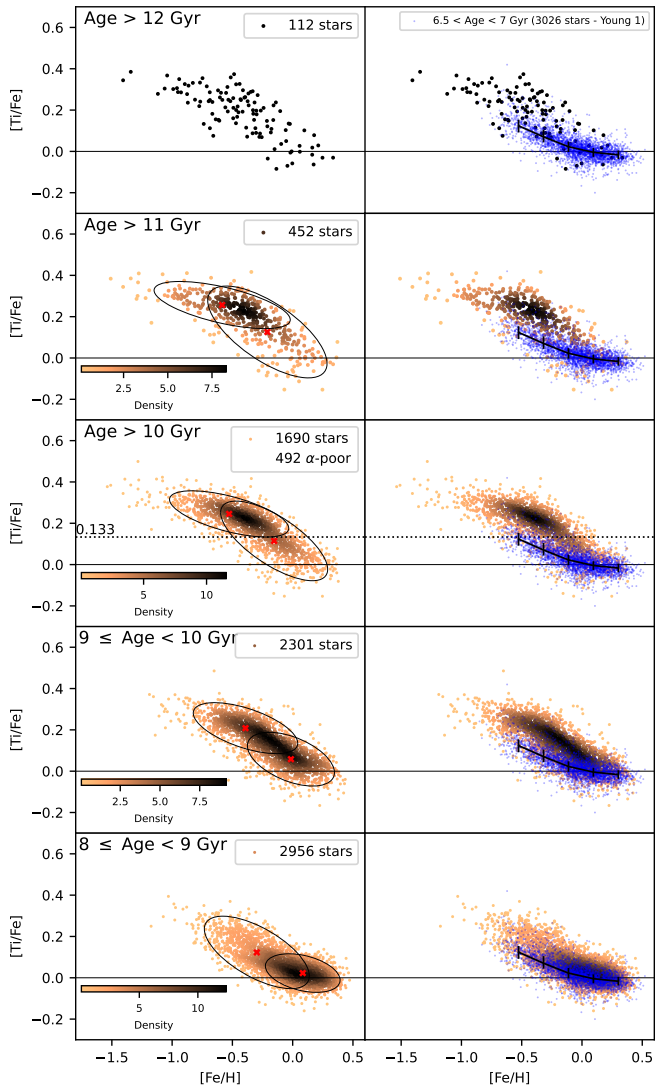

Fig. 6. [Ti/Fe] versus [Fe/H] diagrams. The elements of the plots are the same as in Fig. 5.

ambiguous classifications and are therefore labelled as transition stars. These numbers imply an overall α-poor fraction of approximately 20–30%. The bottom panels of both figures further show that the α-poor population begins to dominate between 8 and 9 Gyr, suggesting a transition in the dominant chemical regime of the thin disc at ~9.5 Gyr.

3.2. Orbital properties

In the previous section, we examined the orbital properties of the old α-rich and α-poor populations identified using the kinematic and dynamical information provided by the GALAH DR4 catalogue. The top-left and top-centre panels of Fig. 7 show the distributions of the α-rich and α-poor populations in the Lindblad diagram for stars older than 10 Gyr, while 6.5–7 Gyr stars from the Young 1 population are shown in the top-right panel as a reference for the typical thin-disc kinematics. The old α-rich population exhibits a widely dispersed distribution, consistent with thick-disc kinematics (e.g. Li et al. 2018). In contrast, the old α-poor population shows a narrow distribution concentrated in the same energy–L_Z region as the thin disc, as indicated by the 16th and 84th percentiles of the density distributions. These contrasting kinematic properties demonstrate that old α-poor stars are virtually dynamically indistinguishable from the thin disc, while the old α-rich population is consistent with a thick-disc origin, highlighting that chemical separation remains reflected in orbital structure even at the oldest ages probed here.

4. Comparison with Galactic chemical evolution models

The presence of a significant fraction (~25%) of stars older than 10 Gyr with low-α element abundance opens the question of whether current chemical evolution scenarios can predict such stars. For this reason, we consider the two-infall model proposed by Palla et al. (2022).

In brief, the model assumes that the MW disc forms by means of two sequential gas accretion episodes, separated by a 3.25 Gyr delay, normally associated with the chemical thick and thin disc, respectively, relative to the first event. Within the adopted framework, stellar radial migration is also implemented to take into account the observed effect of radial mixing of the stellar population born at different radii (see, e.g. Kordopatis et al. 2015; Feltzing et al. 2020). In particular, the authors followed the parametric implementation described by Frankel et al. (2018, see Eq. (8) in Palla et al. 2022). For all the information and details about the prescriptions and assumptions of the adopted model, we refer the reader to Palla et al. (2022). To perform a fair comparison between the model predictions and the old population selected within GALAH, we take into account the cuts in $T_{\rm eff}$ and log g by applying PARSEC (v1.2s) + COLIBRI (s37) tracks. Moreover, we took into account uncertainties in stellar age and abundance determinations by building a 'synthetic' chemical evolution model, namely a mock stellar catalogue of surviving stars. In particular, we add at each model timestep a random error to the ages and the [Fe/H] and [Mg/Fe] abundances of the stars, which have a Gaussian distribution with standard deviation as typical uncertainties of stars.

The result of the comparison between the two-infall framework and the data presented in this work is displayed in Fig. 8. We show the [Mg/Fe] versus [Fe/H] synthetic model predictions and data for observed stars older than 10 Gyr[3]. The figure shows that in this scenario, it is indeed possible to have α-poor stars with disc-like properties that are very old, making our selection of old α-poor candidates fully plausible. In addition, predicted number counts for the low-α population (red points in Fig. 8) represent around 40% of the entire model population older than 10 Gyr, a value larger but still in line than the ~20–30% shown by observations.

However, additional considerations must be taken into account. In the usual picture, the two gas accretion episodes in the two-infall framework are associated with the high-α and low-α sequences, respectively. However, this 'classical' picture is altered in the presence of stellar migration for ages ~10 Gyr, especially for the contribution of the inner disc regions. Indeed, the bursty star formation in these regions of the disc, together with the possible infall pre-enrichment (see Palla et al. 2020; Spitoni et al. 2021 for more details), permit high-α stars to form even after the beginning of the second infall episode. This is shown in Fig. 9, where we label the model mock data associated

[3] We do not perform a data-model comparison for [Ti/Fe]–[Fe/H], due to the long-standing problem in stellar nucleosynthesis of obtaining reliable yields for Ti (see Romano et al. 2010; Prantzos et al. 2018; Pepe et al. 2025).

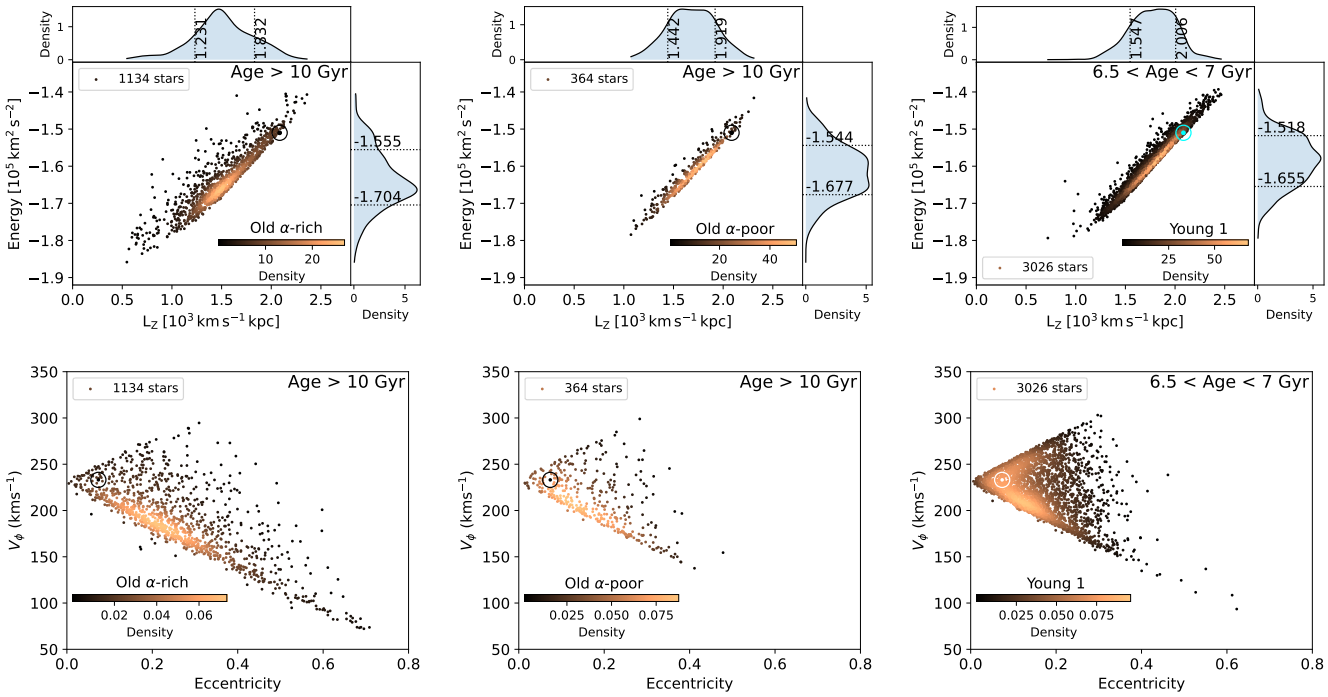

Fig. 7. Dynamical properties of the old and young populations. *Top panels*: Lindblad diagrams for α-rich stars older than 10 Gyr (left panel), α-poor stars older than 10 Gyr (centre panel), and the solar-age stars ($5.1 \leq$ age ≤ 5.5 Gyr) of the *Young 1* population in Fig. 4 (right panel); i.e. blue dots in Figs. 5 and 6. Point colours follow the corresponding colour bars. Marginal density distributions are shown above and to the right of each diagram; dotted lines indicate the 16th and 84th percentiles. The solar position is marked by $\odot$. *Bottom panels*: Rotational velocity (V_ϕ) versus eccentricity. Symbols are the same as in the top panels.

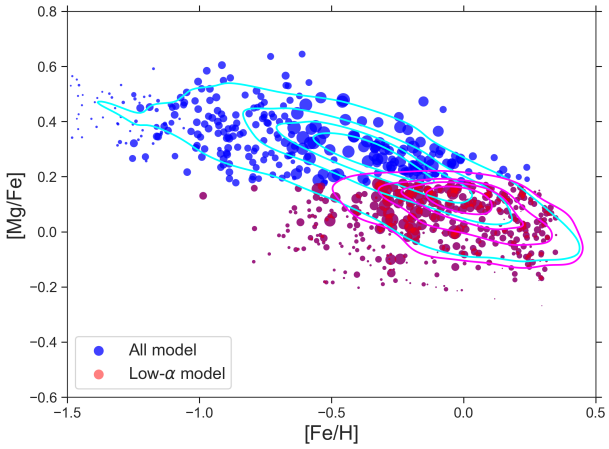

Fig. 8. Two-infall model predictions for [Mg/Fe] vs. [Fe/H]. Coloured points are the synthetic model predictions for stars older than 10 Gyr, with red points being compatible with the old-α poor population defined in Section 3.1. Point size is proportional to the number of stars formed in the model timestep. Cyan and magenta contours represent density lines of the full sample of stars older than 10 Gyr and the α-poor population older than 10 Gyr.

with the first and second infall episodes. It can be clearly seen that the predicted stars associated with the second gas accretion episode can also be associated with high-α stars, with such stars likely migrating from the inner regions. To better highlight this feature, in the Fig. 9 (right panel) we highlight with a different colour predicted mock stars coming from regions inner than the solar radius (R$\simeq$ 8 kpc). In addition, Fig. 9 also shows that mock data associated with the first infall episode can be identified with low-α data, with the tail of the first star-formation episode producing such low-α, high-metallicity ([Fe/H]$\gtrsim$0 dex) stars. It is worth noting that such combined features can explain the presence of both low-α and high-α stars across different time bins (see Fig. 5 for Mg), considering (i) the smooth transition towards lower [α/Fe] and larger [Fe/H] during the first infall and (ii) the simultaneous presence of both high-α and low-α stars after the onset of the second infall, as due to the mixing of stars born in different (radial) regions of the disc.

The adoption of such a detailed model of Galactic chemical evolution already provides important pieces of information on the history of star formation of the early Galactic disc, proposing a possible scenario for the chemical evolution of the old MW disc and highlighting the crucial role covered by stellar radial migration in the Galaxy (e.g. Minchev et al. 2018; Ratcliffe et al. 2023; Chen et al. 2026). However, more in-depth analysis is certainly needed to better investigate the chemical enrichment of the analysed stellar sample, including a comparison between different proposed frameworks in the context of Galactic chemical enrichment (e.g. Sharma et al. 2021; Grisoni et al. 2026). This will be done in future work, possibly taking advantage of spectroscopic follow-up within the sample, exploiting several classes of chemical elements from different enrichment processes on different timescales.

5. Summary and conclusions

Building on the GALAH DR4 catalogue (Buder et al. 2025), we characterised a sample of old SGB stars with reliable age estimates, typically precise to 0.5–0.8 Gyr, based on accurate $T_{\rm eff}$ determinations and distances from *Gaia* parallaxes. We find that stars with solar-like metallicities and low [α/Fe] are present up

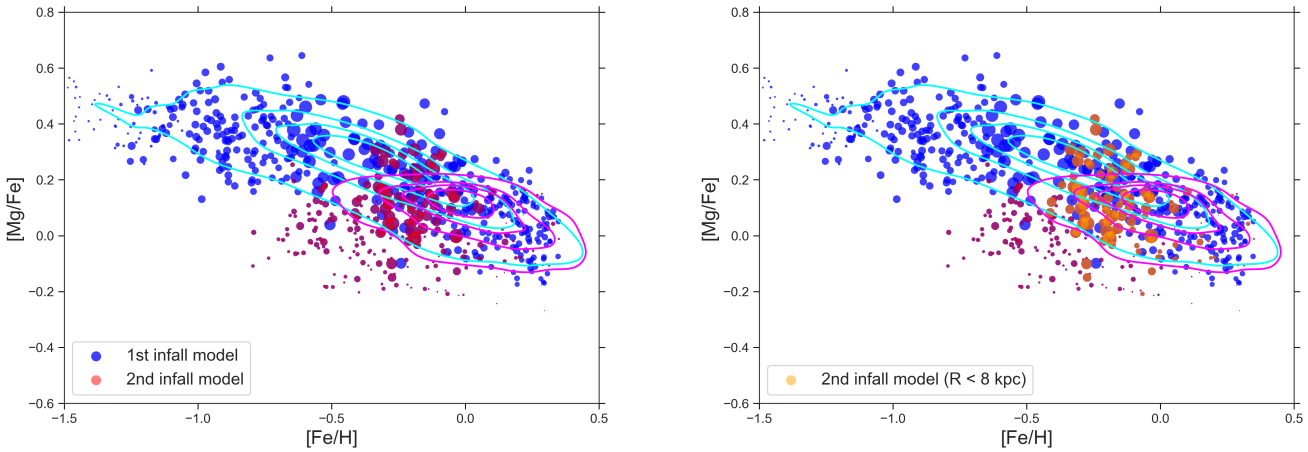

Fig. 9. Two-infall model predictions for [Mg/Fe] vs. [Fe/H]. *Left panel*: coloured points are the synthetic model predictions for stars older than 10 Gyr, with orange points associated with the second gas infall episode, blue points with the first infall. Point size is proportional to the number of stars formed in the model timestep. Data are as in Fig. 8. *Right panel*: same as left panel, but with synthetic model predictions associated with stars with R<8 kpc coloured in orange.

to ≈12.5 Gyr, confirming the existence of an old α-poor population at metallicities characteristic of the solar neighbourhood. The fractions of high- and low-[α/Fe] stars remain comparable across the 8–12.5 Gyr age range, indicating that the two populations overlap substantially in age. The old low-[α/Fe] stars also exhibit orbital properties compatible with those of younger α-poor stars typically associated with the thin disc.

We provide a catalogue of stars older than 10 Gyr selected for spectroscopic follow-up. These targets are sufficiently bright (V < 14 mag) for moderate-quality spectroscopy. Given their ages, metallicities, and location in the SGB region, a subset of these stars are likely to be old solar analogues, i.e. stars that formed with atmospheric properties broadly similar to those of a newborn Sun and have since evolved away from their zero-age main-sequence positions. Detailed spectroscopic characterisation of these targets will allow us to test their chemical composition and investigate whether solar-like stellar environments were already present during the early stages of thin-disc formation.

Together, these results establish the presence of a previously underexplored old α-poor solar-metallicity population and provide a well-defined set of targets for further spectroscopic investigation, opening new avenues for constraining the formation and evolution of the Galactic thin disc. In particular, the identification of candidate old solar analogues provides a direct observational pathway to investigate how early solar-like chemical conditions were established in the MW.

We compared the observed population with detailed chemical evolution models for the MW disc (Palla et al. 2022), finding that α-poor stars can indeed be very old and coeval with the α-rich population in the tested evolutionary framework. Nevertheless, more detailed chemical analyses and comparison with diverse scenarios for Galactic evolutionary models are required to fully characterise the sample nucleosynthetic history and to understand its role in the early evolution of the Galactic disc.

Data availability

The stars selected in this work, together with their ages and other stellar parameters, are publicly available through Zenodo[4].

Acknowledgements. The authors thank V. D'Orazi for discussions and support to the manuscript. The authors thank Jose Schiappacasse Ulloa for discussions and support with data collection. The authors thank the two anonymous referees for constructive feedback that improved the clarity of the paper. R.E.G. and L.M. acknowledge support from INAF through the Large Grants EPOCH and WST, funding for the WEAVE project, the Mini-Grants Checs (1.05.23.04.02), and financial support under the National Recovery and Resilience Plan (PNRR), Mission 4, Component 2, Investment 1.1, Call for tender No. 104 published on 2 February 2022 by the Italian Ministry of University and Research (MUR), funded by the European Union – NextGenerationEU, through the Project 'Cosmic POT' (Grant Assignment Decree No. 2022X4TM3H, MUR). M.P. acknowledges support from HORIZON-INFRA-2024-DEV-01-01 – Research Infrastructure Concept Development, through the project WST: The Wide-Field Spectroscopic Telescope (Grant No. 101183153). Use was made of the Simbad database, operated at the CDS, Strasbourg, France, and of NASA's Astrophysics Data System Bibliographic Services. This research used Astropy[5], a community-developed core Python package for Astronomy (Astropy Collaboration 2018). This work presents results from the European Space Agency (ESA) space mission Gaia. Gaia data are processed by the Gaia Data Processing and Analysis Consortium (DPAC). Funding for the DPAC is provided by national institutions, in particular the institutions participating in the Gaia MultiLateral Agreement (MLA). The Gaia mission website is https://www.cosmos.esa.int/gaia. The Gaia archive website is https://archives.esac.esa.int/gaia.

References

Adibekyan, V. 2019, Geosciences, 9, 105
Amelin, Y., Kaltenbach, A., Iizuka, T., et al. 2010, Earth Planet. Sci. Lett., 300, 343
Astropy Collaboration (Price-Whelan, A. M., et al.) 2018, AJ, 156, 123
Bailer-Jones, C. A. L., Rybizki, J., Fouesneau, M., Demleitner, M., & Andrae, R. 2021, AJ, 161, 147
Baumgardt, H., & Vasiliev, E. 2021, MNRAS, 505, 5957
Bazot, M., Ireland, M. J., Huber, D., et al. 2011, A&A, 526, L4
Bensby, T., Feltzing, S., & Oey, M. S. 2014, A&A, 562, A71
Beraldo e Silva, L., Debattista, V. P., Nidever, D., Amarante, J. A. S., & Garver, B. 2021, MNRAS, 502, 260
Blackwell, D. E., Shallis, M. J., & Selby, M. J. 1979, MNRAS, 188, 847
Blackwell, D. E., Petford, A. D., & Shallis, M. J. 1980, A&A, 82, 249
Borbolato, L., Rossi, S., Perottoni, H. D., et al. 2025, ApJ, 994, 126
Bressan, A., Marigo, P., Girardi, L., et al. 2012, MNRAS, 427, 127
Buder, S., Sharma, S., Kos, J., et al. 2021, The GALAH+ survey: Third data release
Buder, S., Kos, J., Wang, X. E., et al. 2025, PASA, 42, e051
Cardelli, J. A., Clayton, G. C., & Mathis, J. S. 1989, ApJ, 345, 245
Casagrande, L., Portinari, L., & Flynn, C. 2006, MNRAS, 373, 13
Casagrande, L., Ramírez, I., Meléndez, J., Bessell, M., & Asplund, M. 2010, A&A, 512, A54

[4] https://doi.org/10.5281/zenodo.22954679

[5] http://www.astropy.org

Casagrande, L., Wolf, C., Mackey, A. D., et al. 2019, MNRAS, 482, 2770
Casagrande, L., Lin, J., Rains, A. D., et al. 2021, MNRAS, 507, 2684
Cayrel de Strobel, G. 1996, A&A Rev., 7, 243
Chen, A., Shen, J., Wang, C., & Huang, Y. 2026, MNRAS, 546, stag035
Ciucă, I., Kawata, D., Miglio, A., Davies, G. R., & Grand, R. J. J. 2021, MNRAS, 503, 2814
Ciucă, I., Kawata, D., Ting, Y.-S., et al. 2024, MNRAS, 528, L122
Connelly, J. N., Amelin, Y., Krot, A. N., & Bizzarro, M. 2008, ApJ, 675, L121
Dotter, A., Conroy, C., Cargile, P., & Asplund, M. 2017, ApJ, 840, 99
Faisst, A. L., Liu, L.-J., Dubois, Y., et al. 2026, ApJ, 1004, 22
Feltzing, S., Primas, F., & Johnson, R. A. 2009, A&A, 493, 913
Feltzing, S., Bowers, J. B., & Agertz, O. 2020, MNRAS, 493, 1419
Fitzpatrick, E. L. 1999, PASP, 111, 63
Frankel, N., Rix, H.-W., Ting, Y.-S., Ness, M., & Hogg, D. W. 2018, ApJ, 865, 96
Gaia Collaboration (Brown, A. G. A., et al.) 2018, A&A, 616, A1
Gallart, C., Surot, F., Cassisi, S., et al. 2024, A&A, 687, A168
Gent, M. R., Eitner, P., Serenelli, A., et al. 2024, A&A, 683, A74
Giribaldi, R. E., da Silva, A. R., Smiljanic, R., & Cornejo Espinoza, D. 2021, A&A, 650, A194
Giribaldi, R. E., & Smiljanic, R. 2023, A&A, 673, A18
Giribaldi, R. E., Van Eck, S., Merle, T., et al. 2023, A&A, 679, A110
Green, G. M. 2018, J. Open Source Softw., 3, 695
Green, G. M., Schlafly, E., Zucker, C., Speagle, J. S., & Finkbeiner, D. 2019, ApJ, 887, 93
Grisoni, V., Spitoni, E., & Matteucci, F. 2026, A&A, 710, A395
Hansen, J. T., Casagrande, L., Ireland, M. J., & Lin, J. 2021, MNRAS, 501, 5309
Hardorp, J. 1978, A&A, 63, 383
Hayden, M. R., Bovy, J., Holtzman, J. A., et al. 2015, ApJ, 808, 132
Haywood, M., Di Matteo, P., Lehnert, M. D., Katz, D., & Gómez, A. 2013, A&A, 560, A109
Haywood, M., Di Matteo, P., Lehnert, M. D., et al. 2018, ApJ, 863, 113
Haywood, M., Snaith, O., Lehnert, M. D., Di Matteo, P., & Khoperskov, S. 2019, A&A, 625, A105
Heiter, U., Jofré, P., Gustafsson, B., et al. 2015, A&A, 582, A49
Hidalgo, S. L., Pietrinferni, A., Cassisi, S., et al. 2018, ApJ, 856, 125
Karovicova, I., White, T. R., Nordlander, T., et al. 2020, A&A, 640, A25
Katz, D., Gómez, A., Haywood, M., Snaith, O., & Di Matteo, P. 2021, A&A, 655, A111
Kim, Y.-C., Demarque, P., Yi, S. K., & Alexander, D. R. 2002, ApJS, 143, 499
Kordopatis, G., Binney, J., Gilmore, G., et al. 2015, MNRAS, 447, 3526
Li, C., Zhao, G., Zhai, M., & Jia, Y. 2018, ApJ, 860, 53
Lindegren, L., Bastian, U., Biermann, M., et al. 2021, A&A, 649, A4
Maiolino, R., Nagao, T., Grazian, A., et al. 2008, A&A, 488, 463
Majewski, S. R., Zasowski, G., & Nidever, D. L. 2011, ApJ, 739, 25
Marigo, P., Girardi, L., Bressan, A., et al. 2017, ApJ, 835, 77
Maxted, P. F. L., Miller, N. J., Hoyer, S., et al. 2022, MNRAS, 513, 6042
Meléndez, J., Bergemann, M., Cohen, J. G., et al. 2012, A&A, 543, A29
Miller, N. J., Maxted, P. F. L., & Smalley, B. 2020, MNRAS, 497, 2899
Minchev, I., Anders, F., Recio-Blanco, A., et al. 2018, MNRAS, 481, 1645
Mitschang, A. W., De Silva, G., Zucker, D. B., et al. 2014, MNRAS, 438, 2753
Nepal, S., Chiappini, C., Queiroz, A. B., et al. 2024, A&A, 688, A167
Nissen, P. E., & Schuster, W. J. 2010, A&A, 511, L10
Nordström, B., Mayor, M., Andersen, J., et al. 2004, A&A, 418, 989
O'Donnell, J. E. 1994, ApJ, 422, 158
Oliveira, R. A. P., Souza, S. O., Kerber, L. O., et al. 2020, ApJ, 891, 37
Palla, M., Matteucci, F., Spitoni, E., Vincenzo, F., & Grisoni, V. 2020, MNRAS, 498, 1710
Palla, M., Santos-Peral, P., Recio-Blanco, A., & Matteucci, F. 2022, A&A, 663, A125
Pedregosa, F., Varoquaux, G., Gramfort, A., et al. 2011, J. Mach. Learn. Res., 12, 2825
Pepe, E., Palla, M., Matteucci, F., & Spitoni, E. 2025, A&A, 694, A19
Pérez-Villegas, A., Barbuy, B., Kerber, L. O., et al. 2020, MNRAS, 491, 3251
Planck Collaboration VI. 2020, A&A, 641, A6
Porto de Mello, G. F., da Silva, R., da Silva, L., & de Nader, R. V. 2014, A&A, 563, A52
Prantzos, N., Abia, C., Limongi, M., Chieffi, A., & Cristallo, S. 2018, MNRAS, 476, 3432
Ramírez, I., Allende Prieto, C., & Lambert, D. L. 2013, ApJ, 764, 78
Ramírez, I., Meléndez, J., Bean, J., et al. 2014, A&A, 572, A48
Ratcliffe, B., Minchev, I., Anders, F., et al. 2023, MNRAS, 525, 2208
Riello, M., De Angeli, F., Evans, D. W., et al. 2021, A&A, 649, A3
Romano, D., Karakas, A. I., Tosi, M., & Matteucci, F. 2010, A&A, 522, A32
Salaris, M., Chieffi, A., & Straniero, O. 1993, ApJ, 414, 580
Savaglio, S., Rau, A., Greiner, J., et al. 2012, MNRAS, 420, 627
Schlafly, E. F., & Finkbeiner, D. P. 2011, ApJ, 737, 103
Schlegel, D. J., Finkbeiner, D. P., & Davis, M. 1998, ApJ, 500, 525
Scholte, D., Cullen, F., Carnall, A. C., et al. 2025, MNRAS, 540, 1800
Sharma, S., Stello, D., Buder, S., et al. 2018, MNRAS, 473, 2004
Sharma, S., Hayden, M. R., & Bland-Hawthorn, J. 2021, MNRAS, 507, 5882
Snaith, O., Haywood, M., Di Matteo, P., et al. 2015, A&A, 578, A87
Sommariva, V., Mannucci, F., Cresci, G., et al. 2012, A&A, 539, A136
Soubiran, C., Creevey, O. L., Lagarde, N., et al. 2024, A&A, 682, A145
Spina, L., Meléndez, J., Karakas, A. I., et al. 2018, MNRAS, 474, 2580
Spitoni, E., Verma, K., Silva Aguirre, V., et al. 2021, A&A, 647, A73
Spitoni, E., Palla, M., Magrini, L., et al. 2025, A&A, 700, A58
Tsantaki, M., Biazzo, K., Zahra Majidi, F., Tautvaisiene, G., & Busa, I. 2026, arXiv e-prints [arXiv:2601.08890]
VandenBerg, D. A., Brogaard, K., Leaman, R., & Casagrande, L. 2013, ApJ, 775, 134
Vasiliev, E., & Baumgardt, H. 2021, MNRAS, 505, 5978
Vincenzo, F., Weinberg, D. H., Miglio, A., Lane, R. R., & Roman-Lopes, A. 2021, MNRAS, 508, 5903
Viscasillas Vázquez, C., Randich, S., Escate Giribaldi, R., et al. 2026, A&A, 714, A45
Xiang, M., & Rix, H.-W. 2022, Nature, 603, 599
Yi, S. K., Kim, Y.-C., & Demarque, P. 2003, ApJS, 144, 259
Zwintz, K., Aerts, C., Tkachenko, A., et al. 2026, arXiv e-prints [arXiv:2604.04042]

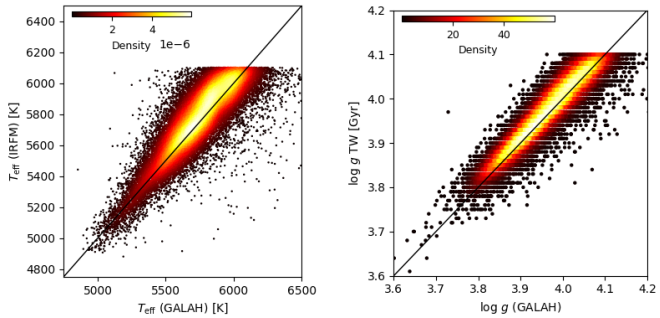

Fig. A.1. Comparison of $T_{\rm eff}$ and log g scales. The dispersion in the plots correspond to the characterised sample selected in Sect. 2.3.

Appendix A: Compatibility between parameter scales

Left panel in Fig. A.1 shows the compatibility between the IRFM $T_{\rm eff}$ scale of GALAH DR3 (Casagrande et al. 2021, used in this work) and the spectroscopic $T_{\rm eff}$ scale of GALAH DR4. The latter is the base of the chemical abundances used in this work. Right panel compares the log g scale derived in this work (related to our age estimates according to Sect. 2.2), with that of GALAH DR4.

Appendix B: Age validation with the cluster NGC 6352

NGC 6352 is an old globular cluster with an age of 10–12.5 Gyr, as inferred from isochrone analyses by VandenBerg et al. (2013) and Oliveira et al. (2020). It has a metallicity of [Fe/H] = −0.55 ± 0.03 dex (Feltzing et al. 2009) and follows a thick-disc-like orbit (Pérez-Villegas et al. 2020). To validate our methodology, we performed both a global isochrone fit in the M_V–$T_{\rm eff}$ plane and individual star-by-star age determinations.

Our analysis is based on the observational compilation of Vasiliev & Baumgardt (2021). Starting from a sample of 3408 stars with Gaia photometry and membership probabilities exceeding 90%, we retained only sources with uncertainties in both Gaia G_{BP} and G_{RP} magnitudes below 0.05 mag. This quality criterion reduced the sample to 2113 stars, of which 751 have membership probabilities above 99%. Photometric $T_{\rm eff}$ were derived from the $G_{BP} - G_{RP}$ colour using the calibrations of Casagrande et al. (2021), which are tied to the IRFM temperature scale established from GALAH DR3 stars. We adopted $G_{BP} - G_{RP}$ in preference to colours involving the G band in order to minimise systematic effects in the $G - G_{BP}$ and $G - G_{RP}$ colour scales (Giribaldi et al. 2023). The calibrations require log g, [Fe/H], and reddening $E(B - V)$ as inputs. We adopted fixed values of [Fe/H] = −0.55 ± 0.10 dex and $E(B - V)$ = 0.24 ± 0.048 mag from Feltzing et al. (2009). The associated uncertainties are needed for the analysis of the errors. The [Fe/H] error reflects typical values in the literature, while the reddening uncertainty was assumed to be of 20%. $E(B - V)$ was transformed into the reddening $E(G_{BP} - G_{RP})$ and the attenuation A_G to derive V_0 via Eq. (D.1) assuming the COD extinction law, as explained in Appendix D. Absolute magnitude M_V was computed as $M_V = V_0 - 5\log(\mathrm{d}) + 5$, where d = 5543 ± 73 pc is the cluster distance (Baumgardt & Vasiliev 2021).

Initial log g estimates were assigned according to Gaia G magnitude: log g = 4 for $G > 18$, log g = 3 for $16 < G \leq 18$, log g = 2 for $14 < G \leq 16$, log g = 1 for $12 < G \leq 14$, and log g = 0.5 for $G \leq 12$. Uncertainties in these preliminary values have only a minor impact on the derived temperatures; for example, an error of 0.5 dex in log g changes $T_{\rm eff}$ by less than 50 K. Refined temperatures were therefore obtained through a second iteration using updated surface gravities. Surface gravities and individual stellar ages (star-to-star henceforth) were derived following the procedure described in Sect. 2.2. Two iterations were performed, with the second adopting the revised $T_{\rm eff}$ values. An α-enhancement of [α/Fe]= +0.2 dex (Feltzing et al. 2009) was assumed via Eq. (1).

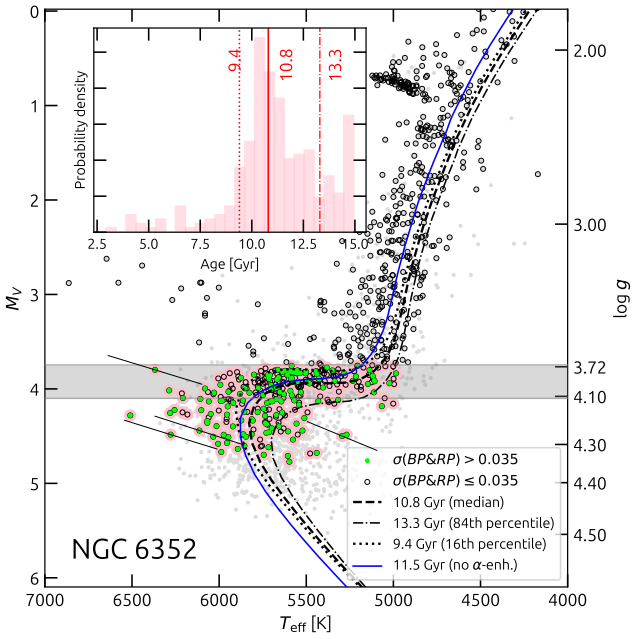

Fig. B.1. M_V–$T_{\rm eff}$ diagram of NGC 6352. Grey and black circles represent cluster stars with membership probabilities higher than 90% and 99%, respectively. Turnoff stars used for the isochrone fitting are highlighted in pink. Stars with photometric precision $\sigma(G_{BP})$ and $\sigma(G_{RP})$ between 0.04 and 0.05 are shown in green. Black lines represent isochrones with ages corresponding to the 16th, median, and 84th quantiles of the histogram. An isochrone with no α-enhancement effect on [Fe/H] is displayed in blue. Oblique lines exemplify changes of positions of a few stars with the most imprecise photometry. The right axis displays the log g scale of isochrone corresponding to the median age. The grey band indicates the subgiant branch at $3.76 < M_V < 4.10$ mag. The inset displays the histogram of the star-by-star age determination. Its median (solid line) and 16th and 84th percentiles (dotted lines and dash-dotted lines) are noted in red.

This validation focuses exclusively on turnoff stars; therefore, we restricted the sample to $17.45 < V_0 < 18.60$ and performed isochrone fitting using a method similar to that described by Giribaldi & Smiljanic (2023). This selection yielded 293 stars with $3.76 < M_V < 4.79$ mag. Figure B.1 presents the M_V–$T_{\rm eff}$ diagram for NGC 6352. Stars with membership probabilities exceeding 99% are shown in black, while the turn-off sample is highlighted in pink. Stars with the most imprecise photometry are shown in green. The dashed line represents the isochrone corresponding to the median of the star-to-star ages, 10.8 Gyr, which is in excellent agreement with the value of 10.75 ± 0.78 Gyr reported by VandenBerg et al. (2013). For comparison, an isochrone computed without α-enhancement effect on [Fe/H] is also shown (blue curve). Its close proximity to the best-fitting solution indicates that neglecting [α/Fe] would lead to an age overestimate of 1 Gyr.

Appendix C: Sources of age uncertainties and biases estimated from analysis of the NGC 6352 cluster

Oblique vectors in Fig. B.1 illustrate the displacements from the combined uncertainties in reddening, photometry, and the colour–$T_{\rm eff}$ calibration. These correspond to $T_{\rm eff}$ uncertainties of 200–250 K for stars with typical photometric precision ($\sigma(G_{BP})$ = 0.029 mag and $\sigma(G_{RP})$ = 0.022 mag) and up to 280 K for those near the adopted quality threshold ($\sigma(G_{BP})$ = $\sigma(G_{RP})$ = 0.05 mag). The $T_{\rm eff}$ uncertainties include contributions from the intrinsic scatter of the colour–$T_{\rm eff}$ calibration (60 K, Table 1 of Casagrande et al. 2021) and reddening uncertainty (∼200 K). The uncertainty in the absolute magnitude, $\sigma(M_V) \simeq 0.15$ mag, is also dominated by the reddening error. It was estimated by adding in quadrature the following sources: (i) the scatter of the Gaia–Johnson colour transformations, $\sigma(V_{calib})$ = 0.03 mag; (ii) the uncertainty of the dereddened magnitude $\sigma(V_0)$ = 0.148 mag = 3.1 × 0.2 × $E(B-V)$, where 0.2 is the 20% error of reddening assumed and 3.1 is the extinction coefficient, and (iii) the cluster distance uncertainty (73 pc), which translates into 0.029 mag through the distance modulus.

The age distribution in Fig. B.1 exhibits an extended tail toward older ages, with the 16th and 84th percentiles corresponding to dispersions of 1.4 and 2.5 Gyr about the median, respectively. This asymmetry contrasts with the distribution of temperature residuals (observational $T_{\rm eff}$ minus isochrone values) computed for the 10.8 Gyr solution, which is symmetric. Namely, it has 16th, median, and 84th percentiles of −291, −2, and +321 K, and a standard deviation of 304 K. This indicates that stars scattered toward cooler temperatures are preferentially mapped into older ages, producing the observed high-age tail the histogram exhibits.

Figure C.1 identifies the stars contributing to the high-age tail. It shows age density distributions for stars located to the cool side of the 10.8 Gyr isochrone in Fig. B.1. The distributions are grouped according to their $T_{\rm eff}$ residuals relative to the isochrone, from the least to the most discrepant intervals, following a colour-code. Additionally, the subgiant branch (SGB) and the turnoff (TO) are separated in the top and bottom panels; a limit of M_V = 4.1 mag (gray band in Fig. B.1) was imposed. The SGB exhibits modest age offsets up to ∼1.5 Gyr for $T_{\rm eff}$ underestimations as large as −400 K. In contrast, the TO shows substantially larger age biases, even for $T_{\rm eff}$ underestimations lower than 100 K. It demonstrates that $T_{\rm eff}$ underestimations in the TO exceeding 100 K, systematically populate the high-age tail of the histogram of Fig. B.1, being largely responsible for inferred ages above the age of the universe 13.7 Gyr.

This analysis indicates that the SGB yields unbiased star-by-star age determinations[6], because at this stage the impact of the $T_{\rm eff}$ deviations from true values nullifies. For the cluster NGC 6352, the SGB remains within 3.72 $\lesssim \log g \lesssim$ 4.10 dex. This effect is also observed in the errors of the star-by-star ages in Fig. C.2, which are minimal (lower than ∼3 Gyr) for $\log g \lesssim 4.1$ dex or $M_V \lesssim 4.1$ mag.

The M_V range of the SGB is primarily determined by stellar age and metallicity. In Sect 2.3, only SGB field stars are present in the sample. Figure C.3 compares the histogram shown in Fig. 4 with with those obtained without the $\log g$ and M_V cuts. The application of these cuts results in a progressively smaller fraction of stars with ages above 10 Gyr. In particular, the fraction of stars older than 12 Gyr decreases from 1.45% in the full sample to 0.87% after applying the $\log g$ <= 4.1 dex cut, and further to 0.38% after the M_V cut. This reduction demonstrates that the $\log g$ and M_V cuts effectively suppress the contribution of stars whose ages are spuriously overestimated due to small underestimations of $T_{\rm eff}$.

[6] This refers to the application of the frequentist approach.

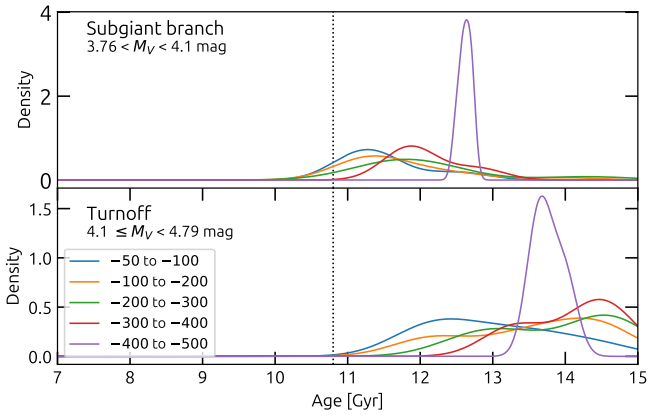

Fig. C.1. Probability density distributions of stellar ages for cluster stars with negative temperature residuals ($\Delta T_{\rm eff} = T_{\rm eff,obs} - T_{\rm eff,iso} < 0$). Stars are grouped according to their temperature residuals, as indicated in the legend, from the least discrepant (−50 to −100 K) to the most discrepant (−400 to −500 K). The top and bottom panels show the SGB and TO stars, respectively, separated according to their M_V values as indicated in the labels. The vertical dotted line indicates the most frequent age of 10.8 Gyr of the star-to-star estimates in Fig. B.1.

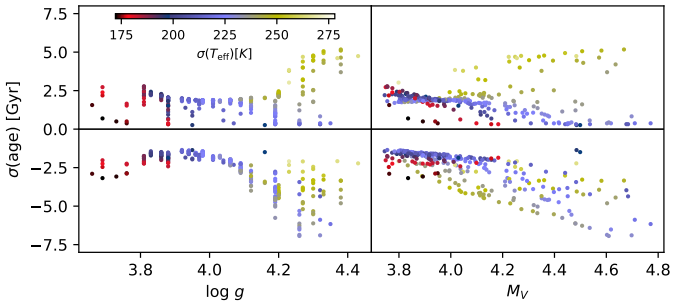

Fig. C.2. Asymmetric age uncertainty of NGC 6352 SGB and TO stars. Values are plotted as functions of $\log g$ and M_V in left and right panels. The colour coding indicates the $T_{\rm eff}$ uncertainty.

Appendix D: Assessment of the impact of reddening on the age estimate

The IRFM $T_{\rm eff}$ adopted in this work is based on intrinsic band magnitudes, whose extinction corrections follow the extinction law of Cardelli et al. (1989) and O'Donnell (1994), hereafter COD. Casagrande et al. (2021) showed that the effect of instead adopting the extinction law of Fitzpatrick (1999) renormalised as per Schlafly & Finkbeiner (2011) (hereafter FSF), becomes significant (i.e. it yields $T_{\rm eff}$ cooler by at least 100 K) for $E(B-V) \gtrsim 0.2$ mag; see Fig. B1 in the paper. Our characterised sample (Sect. 2.3) has a marginal fraction of stars with $E(B-V) > 0.2$ mag, as shown in Fig. D.1. Therefore, if the true reddening of our stars lie somewhere in between COD and FSF estimates, the $T_{\rm eff}$ of our sample would be biased to hotter, leading to somewhat younger ages (see bias map in Fig. 2). Nevertheless, even if it were the case, these age biases would be limited to a minority of 5–10%; see fractions in Fig. D.1. In

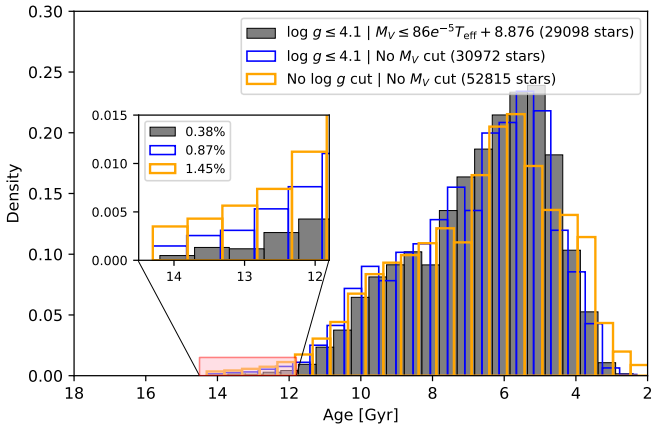

Fig. C.3. Age normalised histograms. The gray, blue, and orange histograms consider the log g and M_V cuts indicated in the legends. The gray histogram is the same as in Fig. 4. The inner plot expands the area shaded in pink. The quantities indicate the percentages of stars older than 12 Gyr in each sample.

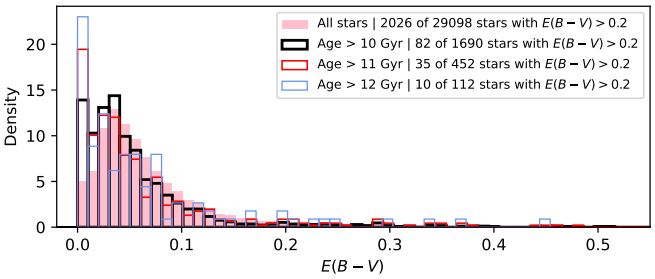

Fig. D.1. Reddening distributions for the characterised sample and its age-selected subsamples. Different colours denote the full sample and the subsamples defined by the adopted age thresholds, as indicated in the legend. The fraction of stars with $E(B-V) > 0.2$ is given for each sample.

any case, since the characterised sample only includes SG stars with log $g < 4.1$ dex, our age estimates are almost insensitive to potential $T_{\rm eff}$ biases, as the values in Figs. 2 and B.1 show.

Our age estimate therefore is primarily influenced by the reddening accuracy via the intrinsic magnitude V_0, which was computed from the Gaia G, G_{BP}, and G_{RP} magnitudes by Eq. (D.1) from Riello et al. (2021):

$$V = G + 0.02704 - 0.01424 \times (G_{BP} - G_{RP}) + 0.2156 \times (G_{BP} - G_{RP})^2 - 0.01426 \times (G_{BP} - G_{RP})^3 \quad \text{(D.1)}$$

where each Gaia magnitude band had previously been corrected for extinction. Such corrections were computed by multiplying $E(B-V)$ by the extinction coefficients R_G, $R_{G_{BP}}$, and $R_{G_{RP}}$, derived using the equations of Table B1 in Casagrande et al. (2021) based on the COD extinction law, for consistence with IRFM $T_{\rm eff}$. We adopted the reddening values in GALAH DR3. For the vast majority[7] of our stars, these were compiled by Casagrande et al. (2021), who selected the values of Green et al. (2019) (Bayestar hereafter) when available, or from Schlegel et al. (1998) (SFD hereafter) re-scaled as in Casagrande et al. (2019).

[7] In the characterised sample, only eight out of 29 098 stars have reddening "rjc", as tagged in GALAH DR3, which refers to the Rayleigh-Jeans colour excess method (Majewski et al. 2011).

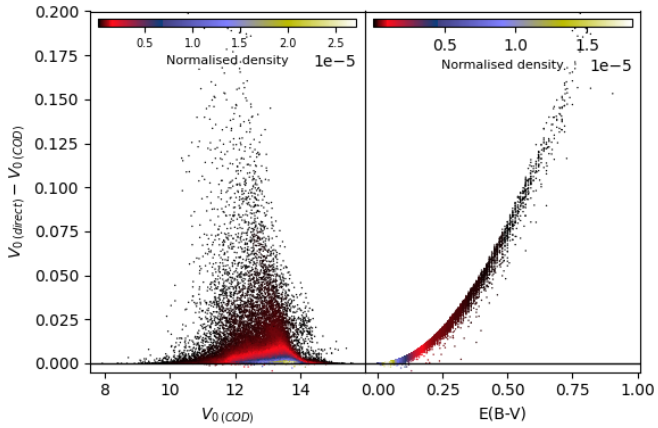

Fig. D.2. Bias of V_0 from correcting extinction on Gaia-transformed V. Values are relative to V_0 derived from G_0 and $(G_{BP} - G_{RP})_0$ in Eq. (D.1) assuming the COD extinction law. Left and right panels show values as function of V_0 and reddening, respectively. The values exhibited correspond to the sample of 91 425 stars with $T_{\rm eff} < 6100$ K (See Sect. 2.3).

The equations for deriving the extinction coefficients of Casagrande et al. (2021) are calibrated as function of the intrinsic (i.e. reddening-corrected) colour $(G_{BP} - G_{RP})_0$. As recommended by the authors, for optimal results, the extinction coefficients were computed iterating the calculations, starting from $(G_{BP} - G_{RP})_0 \simeq (G_{BP} - G_{RP}) - E(B-V)$; we iterated ten times. We note that computing V_0 from an intuitive direct application of the relation $V - 3.1 \times E(B-V)$ instead of using Eq. (D.1) with extinction-corrected magnitudes carries biases that grow with $E(B-V)$, as exhibited in Fig. D.2.

The top and middle panels of Fig. D.3 show the differences in V_0 and G_0, respectively, between the values computed using the FSF and COD extinction laws. Their nearly identical dispersions indicate that the differences in V_0 are driven almost entirely by those in G_0 through Eq. (D.1). The bottom panel shows that these differences correlate with $E(B-V)$ and follow a power-law relation, with the FSF prescription yielding systematically higher magnitudes. For most stars, the difference in G_0 is smaller than 0.1 mag. According to the quantities in Fig. 2, adopting the FSF prescription instead of COD would result in a positive shift in the inferred ages of SGB stars, with a maximum amplitude of 1 Gyr for $E(B-V) < 0.2$ mag.

For estimating the precision of the GALAH DR3 reddening, required for the estimate of the age error budget, we compared the SFD and Bayestar reddening values extracting the data through the `dustmaps` package (Green 2018). SFD was re-scaled by Eq. (1) of Hansen et al. (2021). Figure D.4 shows that the offset between the two scales and the dispersion increase with $E(B-V)$, as traced by the red line sequence, according to the quantities in the plot legends. The consistency holds within 1σ up to $E(B-V) \sim 0.2$ mag. We attributed half of the dispersion to each scale, the corresponding values of which were thus fitted linearly as function of $E(B-V)$ to obtain the reddening uncertainty as expressed below

$$\sigma(E(B-V)) = 0.033 \times E(B-V) + 0.003. \quad \text{(D.2)}$$

The origin of the systematic offset between the two reddening scales is beyond the scope of this work. We note, however, that, apart from a few outliers, the oldest stars in the characterised sample have $E(B-V)$ values within the range where the

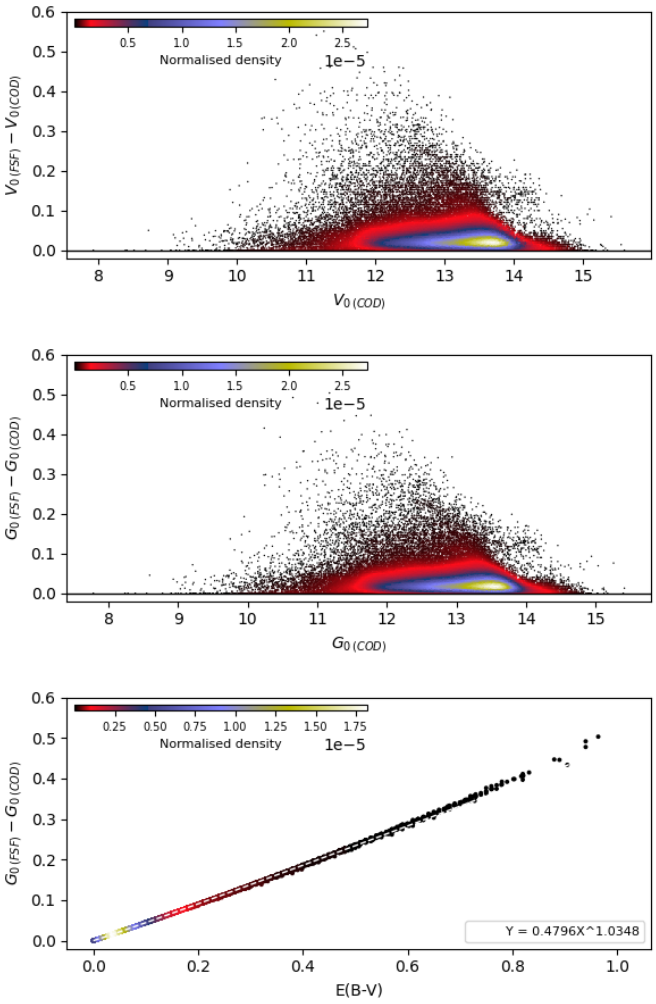

Fig. D.3. Difference between intrinsic magnitudes computed from FSF and COD reddening laws. *Top and middle panels:* The concentration of the distributions are colour-coded according to the bars. *Bottom panel:* Difference of intrinsic G_0 magnitudes as function of reddening. The concentration of the stars is mapped along the horizontal axis and colour-codded according to the bar. The trend is fitted by the white dashed line with a power-law with parameters noted in the plot. The values exhibited correspond to the same sample used in Fig D.2

two scales agree (Fig. D.1), indicating that their derived ages are largely insensitive to potential reddening systematics.

Appendix E: Comparison with catalogued ages

Figure E.1 compares our age estimates with the GALAH 'on-the-fly ages', derived through frequentist inference, and the GALAH BSTEP ages, derived through Bayesian inference (Sharma et al. 2018). Both GALAH age estimates are based on PARSEC+COLIBRI isochrones (Bressan et al. 2012; Marigo et al. 2017). For the range age $\gtrsim$ 5 Gyr, both GALAH age scales exceed our estimates by approximately 2–3 Gyr. The BSTEP ages appear truncated above at 12 Gyr. It is possible that the origin of the discrepancies remain in the different set of isochrones used. However, discrepancies may arise from the diverse details involved in the implementations of the methods and the specific adopted atmospheric, photometric, and astrometric parameters. Therefore, an answer requires a differential analysis. In what regards the age range of interest of this work (> 10 Gyr), our ages

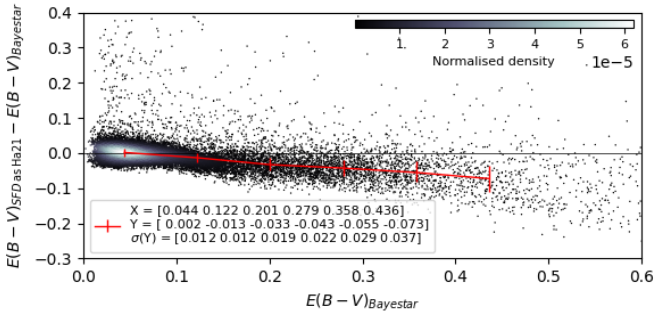

Fig. D.4. Difference between SFD-based and Bayestar $E(B-V)$ values as function of $E(B-V)$. Red lines connect medians computed in equally spaced bins, and vertical bars correspond to 1σ dispersions, their values are indicated in the plot. The values represented by individual points correspond to the sample in Figs. D.2 and D.3 with data available in the Bayestar and SFD maps, and with galactic latitude $|b| > 10°$; this is composed of 35 758 stars.

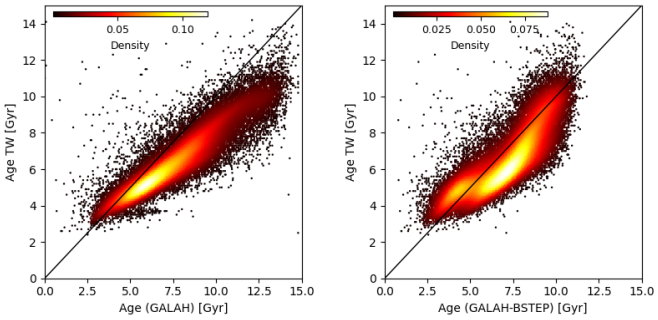

Fig. E.1. Comparison of stellar ages. The plots contain the characterised sample, the age histogram of which shown in Fig. 4. Left and right panels show the 'on-the-fly' and 'BSTEP' ages of the GALAH catalogue in the horizontal axis, respectively.

and the BSTEP ones seem to find better agreement. However, many stars considered 'young' in our sample (i.e. of 5 to 10 Gyr) are found to be older than 10 Gyr by the BSTEP procedure.